Journal of Science and Technology – Engineering and Technology for Sustainable Development
Volume 36, Issue 2, April 2026, 062–069

A Numerical Study on the Train Nose Aerodynamics Using Lattice Boltzmann Method

Nguyen Ngoc Nhi[1,*], Duong Viet Dung[2], Nguyen Dinh Duc[2]
[1]Hanoi University of Civil Engineering, Ha Noi, Vietnam
[2]University of Engineering and Technology, Vietnam National University, Ha Noi, Vietnam
**Corresponding author email: nhinn@huce.edu.vn*

Abstract

The study investigates the aerodynamic performance of high-speed trains by focusing on the influence of nose shape and length on drag at a speed of 97.2 m/s. Utilizing the Lattice Boltzmann Method (LBM), we systematically compare blunt and tapered nose designs to quantify their impact on drag reduction. Our findings reveal that an improved nose geometry significantly reduces aerodynamic drag, which in turn leads to improved operational efficiency, lower energy consumption, and noise reduction. Furthermore, the results indicate that nose length is a critical factor in mitigating both concentrated end-face pressure and vortex drag. The analysis of benchmark models like the Shinkansen E5 and Thalys PBA confirms that a well-designed train nose is paramount for achieving superior aerodynamic performance. This research provides a robust scientific foundation for the design enhancement of future high-speed train designs, ultimately enhancing their speed and efficiency.

Keywords: Aerodynamic drag, Lattice Boltzmann, high-speed train, noise reduction, nose shape.

1. Introduction

In the railway industry, the aerodynamic analysis of trains is fundamental to improving operational performance, reducing energy consumption, and ensuring system safety. As train speeds increase, aerodynamic challenges such as drag, pressure waves, and complex flow structures become particularly significant [1]. Addressing these challenges is not only a matter of technical improvement but also has direct implications for economic feasibility, passenger comfort, and environmental sustainability. This context is especially relevant for Vietnam's upcoming North-South high-speed rail project. For this initiative, aerodynamic improvements are critical for achieving sustainable and efficient transportation, helping to minimize both operational costs and environmental impact. Thus, a thorough understanding of these aerodynamic phenomena is essential for designing more efficient train profiles that reduce drag and for planning infrastructure that is in harmony with the surrounding environment (Fig. 1).

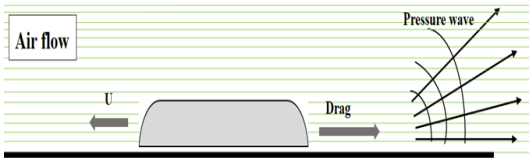

Fig. 1. The aerodynamic problem of the train when moving

Traditionally, the study of high-speed train aerodynamics has relied on experimental methods, including full-scale tests [2], moving model rigs [3], and scaled-model experiments in wind tunnels [4]. While full-scale measurements provide the most realistic data, they are often prohibitively expensive and sensitive to environmental conditions, making them impractical for repeated analysis [2]. On the other hand, scaled-model tests offer better control over experimental conditions, allowing for detailed analysis of flow structures [3, 4]. However, these methods face significant challenges with scaling effects and achieving Reynolds number similarity, which complicates the extrapolation of results to full-scale applications [5].

To resolve these issues, Computational Fluid Dynamics (CFD) has emerged as a powerful tool for simulating complex scenarios, such as wind gusts or passing trains, and providing detailed flow field data [6]. Various CFD models have been applied. Reynolds-Averaged Navier-Stokes (RANS) models, such as the k-ε model, are often used to predict mean flow characteristics but struggle to capture unsteady phenomena [7]. Large Eddy Simulation (LES) can provide high accuracy for turbulent structures but requires immense computational cost, especially at high Reynolds numbers [8]. To balance accuracy and efficiency, hybrid methods like Detached Eddy Simulation (DES) and its improved version Improved

p-ISSN 3093-3242
e-ISSN 3093-3579
https://doi.org/10.51316/jst.189.etsd.2026.36.2.8
Received: May 4, 2025; Revised: Oct 23, 2025
Accepted: Oct 30, 2025; Online: Mar 24, 2026

Delayed Detached Eddy Simulation (IDDES) have been widely used, successfully predicting the slipstream and wake structures of high-speed trains [9].

Among these design factors, the train's nose shape has a decisive influence on its overall aerodynamic performance [10]. It is well-established that changing the nose from a blunt to a streamlined shape is the most effective measure to reduce drag, primarily by mitigating adverse pressure gradients and vortex formation [11]. Furthermore, increasing the nose length helps to reduce peak pressure at the front and minimize the size of wake vortices, which also improves stability against crosswinds or when entering tunnels [10]. These design strategies promote attached, laminar flow and delay flow separation, confirming the critical role of the nose in drag reduction and energy efficiency [11].

This study employs the Lattice Boltzmann Method (LBM) to investigate the effects of nose shape and length on aerodynamic drag, comparing blunt and streamlined designs with reference models such as the Shinkansen E5 and Thalys PBA. By quantifying drag reduction and flow modifications, it provides a scientific basis for advancing future high-speed train designs in Vietnam's North-South corridor, enhancing performance while reducing energy consumption and noise.

The remainder of this paper is organized as follows: Section 2 details the methodology, including the LBM, geometric models, and meshing strategy. In Section 3, we analyze the influence of nose length and shape on aerodynamic characteristics, such as drag force and pressure distribution, using the LBM method. Section 4 presents the conclusions drawn from these findings.

2. Methodology

2.1. Lattice Boltzmann Method

The LBM models fluid dynamics through the evolution of particle distribution functions on a discrete lattice, deriving macroscopic properties such as density and velocity from mesoscopic collision and streaming processes [1]. This approach bypasses direct discretization of the Navier-Stokes equations, offering advantages in computational efficiency, parallelizability, and boundary treatment for complex geometries like train noses.

The core Boltzmann equation for the distribution function f is given by:

$$\frac{\partial f}{\partial t} + \mathbf{c} \cdot \nabla f = \mathbf{\Omega}(f) \tag{1}$$

where $\mathbf{c}$ is the particle velocity and $\mathbf{\Omega}(f)$ is the collision operator. This archetype proficiently consummates the probe's mandates by disentangling labile flows abutting train noses, illuminating pressure inclines and vortical progressions with augmented thriftiness contra orthodox CFD apparatuses [1].

The Bhatnagar-Gross-Krook (BGK) proxy streamlines $\mathbf{\Omega}(f)$ via equilibrium relaxation f^{eq} at a rate determined by the relaxation time τ:

$$\mathbf{\Omega}(f) = -\frac{1}{\tau}(f - f^{eq}) \tag{2}$$

Thus, the discrete Lattice Boltzmann-BGK equation emerges as:

$$f_i(\boldsymbol{x} + \boldsymbol{c}_i \Delta t, t + \Delta t) = f_i(\boldsymbol{x}, t) - \frac{\Delta t}{\tau}\left(f_i(\boldsymbol{x}, t) - f_i^{eq}(\boldsymbol{x}, t)\right) \tag{3}$$

here, i denotes lattice directions. The relaxation parameter τ correlates with kinematic viscosity ν:

$$\nu = c_s^2 \Delta t(\tau - \tfrac{1}{2}) \tag{4}$$

In lattice units, $\Delta t = 1$, and lattice spacing $\Delta x = 1$, and speed sound $c_s = \frac{c}{\sqrt{3}}$ [30], where $c = \frac{\Delta x}{\Delta t} = 1$ is the lattice speed. The equilibrium distribution function f_i^{eq} is calculated as follows:

$$f_i^{eq}(\boldsymbol{x}, t) = w_i \rho \left(1 + \frac{\boldsymbol{u}\cdot\boldsymbol{c}_i}{c_s^2} + \frac{(\boldsymbol{u}\cdot\boldsymbol{c}_i)^2}{2c_s^4} - \frac{\boldsymbol{u}\cdot\boldsymbol{u}}{2c_s^2}\right) \tag{5}$$

where ρ is the macroscopic fluid density and $\boldsymbol{u}$ is the macroscopic fluid velocity. w_i are the weighting factors and $\boldsymbol{c}_i$ are the discrete velocity vectors, which are defined by the lattice model. This study employs the D2Q9 model (2 dimensions, 9 velocity vectors). Specifically, w_i have values of 4/9 for i equal 0, 1/9 for i equal from 1 to 4, and 1/36 for i equal from 5 to 8. The discrete velocity vectors c_i are defined as follows:

$$\boldsymbol{c}_i = \begin{cases} (0,0)c, & i = 0 \\ (\pm 1,0)c, (0,\pm 1)c, & i = 1-4 \\ (\pm 1,\pm 1)c, & i = 5-8 \end{cases} \tag{6}$$

Finally, the macroscopic quantities are recovered by taking the moments of the distribution functions:

$$\rho(\boldsymbol{x}, t) = \textstyle\sum_i f_i(\boldsymbol{x}), \quad \rho\boldsymbol{u}(\boldsymbol{x}, t) = \textstyle\sum_i \boldsymbol{c}_i f_i(\boldsymbol{x}, t) \tag{7}$$

The fluid pressure p is related to the density through the equation of state $p = \rho c_s^2$. Under low Mach number conditions (Ma < 1), density fluctuations are negligible, and therefore, the flow can be treated as incompressible. For particles representing the rigid object, the interpolated bounce-back (IBB) method is employed to replace the streaming procedure. When a fluid particle located at $\boldsymbol{x}_f$ (denoted as boundary cell) has a lattice link along $\bar{\imath}$-direction that is blocked by a solid particle located at $\boldsymbol{x}_s$ (solid cell), the unknown distribution function along opposite direction i is determined by a linear interpolation function using the post-collision distribution function and the adjacent fluid particle located $\boldsymbol{x}_{ff}$ (fluid cell) in i-direction as follows:

$$f_i(\boldsymbol{x}_f, t+\Delta t) = \begin{cases} 2q f_{\bar{i}}^{+}(\boldsymbol{x}_f, t) + (1-2q) f_{\bar{i}}^{+}(\boldsymbol{x}_{ff}, t), & q \le \frac{1}{2}, \\ \frac{1}{2q} f_{\bar{i}}^{+}(\boldsymbol{x}_f, t) + \frac{2q-1}{2q} f_{\bar{i}}^{+}(\boldsymbol{x}_f, t), & q \ge \frac{1}{2}, \end{cases} \quad (8)$$

where $q = \frac{|\boldsymbol{x}_f - \boldsymbol{x}_i|}{|\boldsymbol{x}_f - \boldsymbol{x}_s|}$ is a spatial ratio with x_i indicating the intersection point between the lattice link and boundary curve, as shown in Fig. 2. The normalized output macroscopic variables in LBM are expressed as follows: $\boldsymbol{x}^* = \frac{\boldsymbol{x}}{D}, \boldsymbol{u}^* = \frac{\boldsymbol{u}}{U_0}, \Delta t^* = \frac{\Delta t U_0}{D}$ and $p^* = \frac{p - p_0}{\rho U_0^2}$. The Reynolds number is defined as $Re = \frac{U_0 D}{\nu}$ where U_0, D, and ν denote reference velocity U_0, the characteristic length D, and kinematic viscosity ν in the lattice unit.

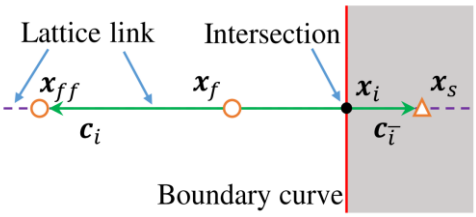

Fig. 2. Sketch of the interpolated bounce-back method

2.2. Drag and Lift Coefficient

Aerodynamic force is the total force generated from the distribution of pressure and friction on the surface of a body. This force can be analyzed into two perpendicular components: Drag, which is the force component parallel to the direction of the oncoming flow, and Lift, which is the component perpendicular to the flow direction (Fig. 3).

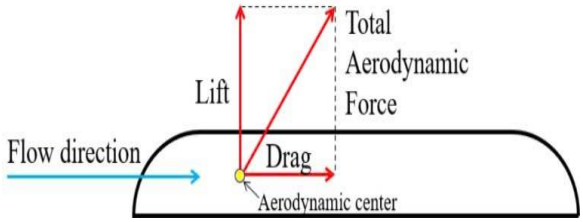

Fig. 3. Distribution of aerodynamic force components

In the numerical analysis, the total fluid forces acting on the 2D rigid body's surface, $[\boldsymbol{F}(F_x, F_y)]$, are computed by the momentum exchange method on the boundary cell layer. These forces are then non-dimensionalized to yield global aerodynamic coefficients, which enable performance comparisons between different designs. The lift (C_L) and drag (C_D) coefficients are defined as follows:

$$C_L = \frac{F_y}{\frac{1}{2}\rho U_0^2 D}; \quad C_D = \frac{F_x}{\frac{1}{2}\rho U_0^2 D} \quad (9)$$

where F_x and F_y are the drag and lift forces, respectively.

2.3. Geometric Model

The computational domain and boundary conditions are shown in Fig. 4. A no-slip boundary condition was applied to the train surface. To simulate the ground effect, the top (AB) and bottom (CD) boundary of the domain were modeled as a moving wall with the same velocity as the incoming flow $(U_0 = 97.2\ m/s)$, representing the relative motion between the train and the ground. The velocity inlet (AC) was set to a uniform flow, and a pressure outlet condition was used for the downstream boundary (BD).

Boundary Line	Crosswind
AC	Velocity inlet
BD	Pressure inlet
AB, CD	Moving wall

Part	Content	Color
1	First layer mesh	
2	Sencon layer mesh	
3	Train	

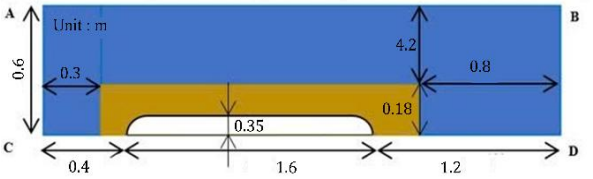

Fig. 4. Schematic of the computational domain, illustrating the boundary conditions and mesh region structure used in the simulation

The Cat Linh – Ha Dong train model was chosen as the base model for the simulation. The length of the train is L equal 1.6 m, and the train has a height of H equal 0.35 m. The train has a blunt nose shape (Fig. 5). Therefore, the model test sets the length of the train's nose at 0.005 m and the shape of the nose as elliptical. To evaluate the impact of the train's nose length, experiments were conducted by varying the train's nose length from 0.005 m to 0.1 m.

Fig. 5. The blunt train's nose of the Cat Linh - Ha Dong train

Besides, the study has conducted data matching with train models that have more complex profiles and are

widely used around the world, such as Japan's Shinkansen E5 model and the Thalys PBA from Germany (Table 1). The influence of length on aerodynamic performance, including drag coefficient, nose pressure distribution, surrounding flow structure, and the impact of changes in vortex turbulence size, has been analyzed and compared.

Table 1. Train configuration

Model	Model name	Nose length (m)	Inflow (m/s)
	NL0.5	0.005	97.2
	NL2	0.02	97.2
	NL5	0.05	97.2
	NL10	0.1	97.2
	Shinkansen E5	0.15	97.2
	Thalys PBA	0.15	97.2

2.4. Mesh

Standard LBM models are traditionally most effective on a single grid level. However, to accurately and efficiently simulate the flow near the train's surface (boundary layer), this study applies a static adaptive mesh refinement method. This approach allows for local mesh refinement by using finer mesh layers near the train's surface, while maintaining a coarser mesh in the far-field regions.

The mesh division method used is an unstructured mesh or triangular plate. The size of the survey domain is presented in Fig. 6. The mesh is densely compressed near the train to accurately calculate the flow changes. The mesh near the train is compressed to a size of 1×10^{-6} m, while the mesh in the outer region has a size ranging from 8×10^{-4} to 1×10^{-5} m. The mesh is divided into approximately 400,000 mesh points (Table 2).

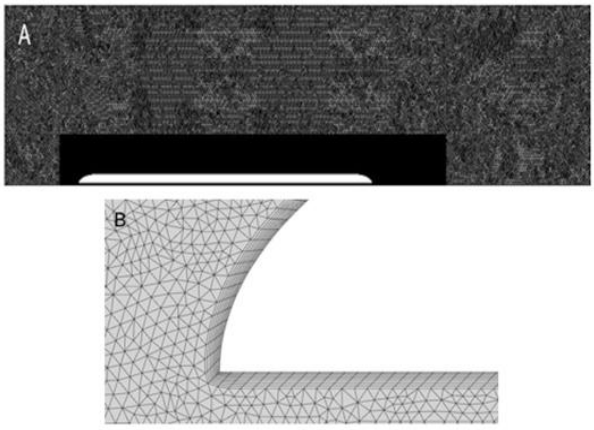

Fig. 6. Mesh of the simulated area: A) Full mesh obstruction; B) The first layers of the mesh

Table 2. Number of mesh points of the train model

Model name	Nodes	Element size ($\times 10^{-6}$ m)	First layer thickness ($\times 10^{-8}$ m)	Y+
NL0.5-BR0	378 423	8	8	5.3975
NL2-BR0	384 622	10	8	5.6874
NL5-BR0	405 736	8	8	5.6171
NL10-BR0	378 430	10	8	5.5050
Shinkansen E5	382 229	10	8	5.4087
Thalys PBA	390 004	8	8	5.6040

To determine a suitable number of mesh points, the study increased the number of mesh points to 600,000 and found that the results did not change much. Therefore, the study decided to keep the original number of mesh points to suit the computer's processor. The *Y+* value for most cases falls within the range of 5.4 to 5.7.

The mesh is divided according to the following five criteria.

1. The mesh points are the points that assign 4 values of the flow field.

2. The distribution of the wall-adjacent region must be fine enough (suitable for the computer's memory) to monitor the flow moving around the boundary layer. The thickness of the boundary layer for turbulent flow is calculated using the formula:

$$\delta(x) = 0.37 \times \frac{x}{Re^{\frac{1}{5}}}. \quad (11)$$

3. If the boundary region does not have enough mesh points captured, the outer region will exhibit incorrect dynamic behavior.

4. The mesh in the distant region will gradually become sparser to save memory for the computer.

5. The mesh cells are perpendicular to each other. If the mesh cells do not ensure orthogonality or exhibit distortion, it will cause the calculation results to be inaccurate. To evaluate the quality of the mesh, we rely on the Skewness and Orthogonal parameters of the mesh, which will be examined in Table 3. The Skewness and Orthogonal indices are used to evaluate the deviation of the grid element's shape from the ideal shape. Specifically, a Skewness value of 0 indicates that the mesh shape meets the ideal standard, with triangular meshes being equilateral triangles. Skewness index within the range of 0 to 0.8 will ensure good mesh accuracy. For the Orthogonality index, a value range from 0.2 to 1 indicates good mesh quality. Therefore,

according to the group's mesh parameter evaluation results in Table 3, the calculation results ensure high accuracy.

Table 3. Mesh quality assessment parameter

Parameter	Min	Max	Average
Skewness	1.3057×10^{-10}	0.75	0.11
Orthogonal	0.47	1	0.93

3. Calculation and Analysis Results

3.1. Aerodynamic Analysis

To reduce the drag affecting the train's nose, simulations of the nose length were conducted. The configurations NL0.5, NL2, NL5, NL10, Thalys, and Shinkansen E5 were analyzed to examine the impact of the nose length on the train (Table 4).

Table 4. The coefficients C_D, C_L, C_L/C_D of each train

Train	D (N)	L (N)	C_L	C_D	C_L/C_D
NL0.5	56.1	1265.82	0.53	0.67	1.26
NL2	33.09	1390.85	0.31	0.74	2.39
NL5	25.14	1469.41	0.25	0.77	3.08
Thalys PBA	23.51	1496.75	0.23	0.81	3.52
Shinkansen E5	21.61	1561.81	0.2	0.82	4.10

3.1.1. Drag

The total drag force decreases significantly when the nose length of the train increases from 0.005 m to 0.1 m, with slight variations between the nose shapes of the Thalys and Shinkansen E5 (Fig. 7). The total drag force of the train with a nose length of 0.005 m decreased by up to 50%. However, the drag does not decrease linearly. The resistance decreases rapidly in the range of 0.005 m to 0.2 m and decreases slightly in the range of 0.005 m to 0.1 m, compared to the length of the nose.

The viscous drag is almost constant at any nose length. The pressure drag is related to the surface pressure distribution. Therefore, the surface pressure distribution is compared with the configurations (NL0.5; NL2; NL5; NL10; Thalys; and Shinkansen E5) shown in following sections. If the nose length becomes longer, the nose is changed from a blunt tip to a streamlined shape. Due to the change in shape to a more streamlined form, the high-pressure area of the nose is reduced towards the train's stern. The rapid change in pressure distribution due to the low-pressure region is manifested in the blunt nose. On the other hand, the smooth variation of pressure distribution is represented by the pointed nose.

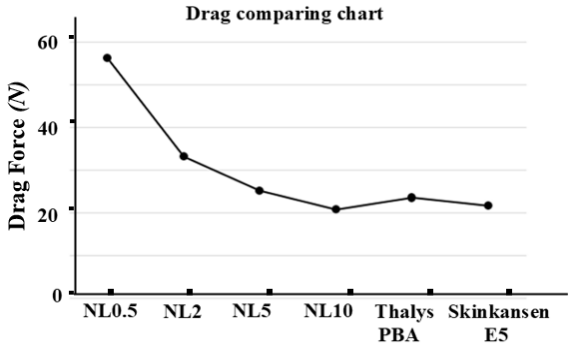

Fig. 7. Comparison of drag force (N) for different train nose designs. The chart shows a clear reduction in aerodynamic drag as the nose shape becomes more streamlined, with the Shinkansen E5 model exhibiting the lowest resistance

3.1.2. Drag coefficient (C_D) and lift coefficient (C_L)

The characteristics of the drag coefficient of the train with different lengths are shown in Fig. 8. It can be seen that the total drag coefficient of the streamlined lengths ranges from 0.005 m to 0.1 m. The total drag coefficient decreases as the length of the nose increases. However, it may only be applicable within a certain range. Since when the length changes from 0.005 m to 0.2 m, the drag coefficient decreases by 41.5%, but only decreases by 25% when the length changes from 0.005 m to 0.1 m. For the nose shapes of the Thalys PBA and Shinkansen E5 trains, the drag coefficient decreases slightly from 0.23 (Thalys PBA) to 0.2 (Shinkansen E5), which is a reduction of 13%.

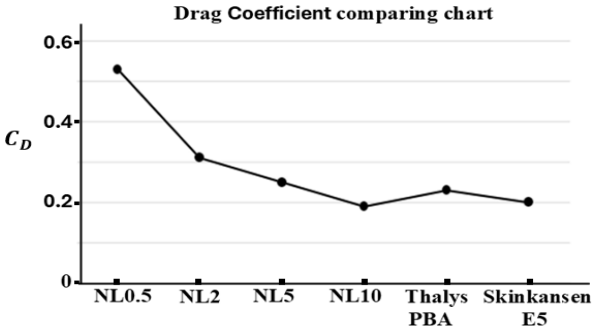

Fig. 8. Comparison of drag coefficient (C_D) for different train nose designs

Increasing the length of the train's nose has a significant impact on the lift coefficient C_L of the train, allowing it to move faster. Fig. 9 shows that increasing the length of the nose is an effective method to enhance the lift force on the train. Increasing the length of the nose from 0.005 m to 0.1 m results in a slight increase of 18.57%. A longer nose generally produces a higher lift coefficient, which is a key factor influencing the train's stability at high-speed

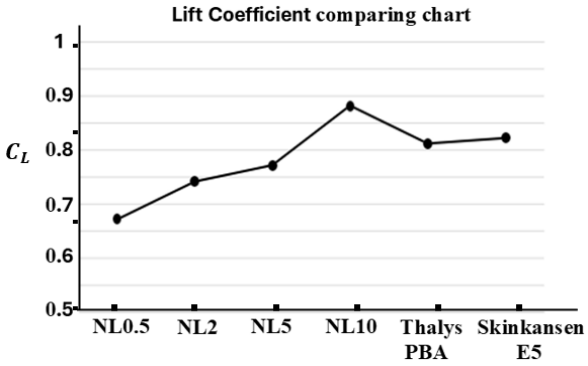

Fig. 9. Lift coefficient (C_L) for various train nose designs.

3.1.3. Aerodynamic coefficient (C_L/C_D)

Lift and drag are both aerodynamic forces, and the ratio of lift to drag (L/D or C_L/C_D) is an indicator of the aerodynamic efficiency of a high-speed train. For high-speed trains, the C_L/C_D ratio is significant in evaluating the train's performance and efficiency under operating conditions. The higher the C_L/C_D ratio, the more it helps reduce drag conditions during movement. When the C_L/C_D ratio is high, the train can move faster and save more energy while also reducing drag and noise generated. Indeed, the C_L/C_D ratio is significant in the design and improvement of high-speed train performance.

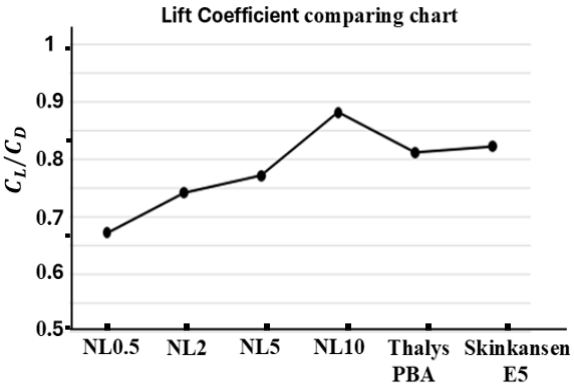

Fig. 10. Aerodynamic efficiency coefficient (C_L/C_D) of different train nose designs

As shown in Fig. 10, the aerodynamic coefficient of the NL0.5 train is only 1.26 (Table 4), but when we change the nose length to NL10, the aerodynamic coefficient increases to 4.63, which is 3.6 times increased. This proves that increasing the length of the train's nose can improve the airflow around the nose, reducing air pressure and drag. As a result, with a longer nose, the drag coefficient (C_D) can decrease, facilitating a relatively stable or increased lift force (C_L). When comparing the NL10 nose with the Thalys PBA and Shinkansen E5 noses, the aerodynamic coefficient decreases slightly, possibly due to various geometric factors of the actual noses that are difficult to replicate in the NL10. It will have to examine other factors such as pressure and the flow field around the train to make a comprehensive assessment.

3.2. Analysis of the Pressure Acting on the Train's Nose

The rapid change in pressure distribution due to the low-pressure area is represented by a blunt nose. On the other hand, the smooth variation of pressure distribution is represented by the tapered nose.

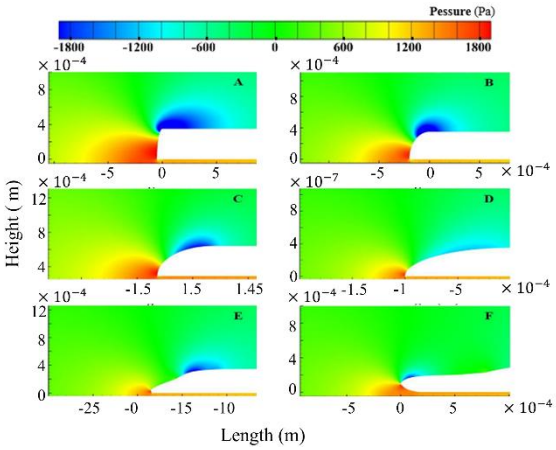

Fig. 11. Pressure distribution at the train's nose for various designs: A) NL0.5; B) NL2; C) NL5; D) NL10; E) Thalys PBA; F) Shinkansen E5.

Fig. 11 shows the flow structure around the train's nose with different lengths and shapes. It can be seen that the size of the positive pressure region at the NL0.5 nose is very large due to the short nose. However when increasing the length of the nose from 0.005 m to 0.1 m, this pressure area gradually shrinks towards the nose tip. This is consistent with the calculated data showing that the drag coefficient decreases as the length of the train's nose increases. With the two shapes of the Thalys PBA and Shinkansen E5 trains, this pressure zone is very small and only appears at the front of the train. Changing the shape of the train's nose from an ellipse to the design of the Thalys PBA and Shinkansen E5 also significantly reduces the pressure acting on the train.

The upper part of the train's nose can see a region of negative pressure appearing, caused by the significant flow separation due to the large change in the train's shape slope, leading to the formation of a large negative pressure. The negative pressure region varies with the change in the length of the train's nose from 0.005 m to 0.1 m, possibly due to the flow at the tip of the long nose, which helps block and reduce the airflow beneath the nose. This phenomenon can be used to explain why the aerodynamic drag of a short-nosed train is greater than that of a long-nosed train. When comparing the two shapes of the Thalys PBA and Shinkansen E5 trains, the

negative pressure regions appear extremely small and minor. Especially at the nose of the Shinkansen E5, it only appears at the tip of the train and has a very narrow pressure zone. This explains the aerodynamic effective design of the Shinkansen's nose shape.

3.3. Analysis of the Flow around the Train's Stern

The flow field of the vortex around the train's stern has a significant impact on the variation of aerodynamic forces and the train's pressure. The pressure drag is related to the distribution of surface pressure. If the length of the train's nose becomes longer, the nose is changed from straight to streamlined. Due to the change in the streamlined shape, the high-pressure area of the nose is reduced to stern pressure.

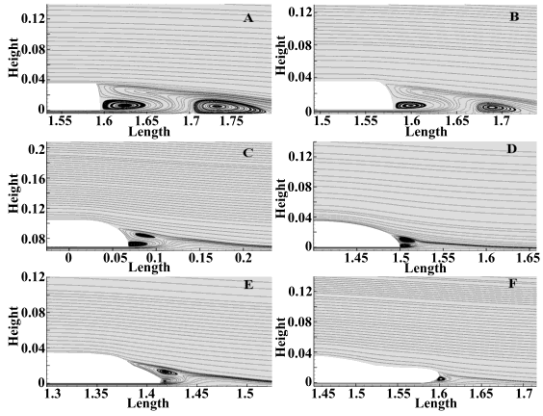

Fig. 12. Analysis of wake vortex behind the train's stern for different designs: A) NL0.5; B) NL2; C) NL5; D) NL10; E) Thalys PBA; F) Shinkansen E5

The vortex appears behind the train (Fig. 12) shows the pressure difference between the front and the stern of the train. The smaller the vortex, the less the pressure, which indicates that the pressure drag acting on the train is reduced. The reduction in pressure drag will decrease the total drag acting on the train because pressure drag accounts for up to 80% of the total drag.

When changing the length of the train's nose from 0.005 m to 0.2 m the vortex size only decreases by 35%, but when increasing the nose length from 0.02 m to 0.1 m, the vortex size decreases by up to 70%. The pressure difference between the nose and stern of the train is greatly reduced. It means that the flow through the train is smoother at the tapered nose, as the shape gradually changes. Therefore, the pressure drag between the nose and the stern of the train decreases. When comparing the NL10 train with the Thalys PBA and Shinkansen E5, the vortex size decreases by 22% and 68%, respectively. It can be seen that the vortex appearing on the Shinkansen E5 train is extremely small and only occurs behind the stern of the train.

4. Conclusion

This study confirms that a train's nose shape is a critical factor for mitigating aerodynamic drag, a key consideration for the design and operational efficiency of high-speed rail. Our LBM simulations reveal a direct correlation between increased nose length and the reduction of both pressure and vortex drag, with longer, more tapered designs demonstrating superior performance. The analysis of benchmark models like the Shinkansen E5 and Thalys PBA validates these findings, highlighting that a well-designed nose is essential for achieving exceptional aerodynamic performance.

Based on these results, we provide a clear recommendation for the design of the upcoming North-South high-speed railway in Vietnam. It is crucial that the project adopts a long, tapered nose shape, similar to the highly effective Japanese Shinkansen E5 model, to minimize aerodynamic resistance. A carefully engineered nose will not only enhance the train's top speed and energy efficiency but also play a vital role in reducing operational noise, thereby improving overall ride quality. This research offers a data-driven guide for the future of high-speed train development in the country.

Acknowledgement

This research is funded by Vietnam National Foundation for Science and Technology Development (NAFOSTED) under grant number 107.03-2024.16

References

[1] K. He, Q. Huang, G. Chen, B. Pei, N. Huang, and S. Krajnović, Large eddy simulation of reynolds number impact on streamlined high-speed train flows, Physics of Fluids, vol. 36, Dec. 2024, Art. no. 125134. https://doi.org/10.1063/5.0245055

[2] T. Takaishi and M. Ikeda, Experimental method for wind tunnel tests to simulate turbulent flow on the roof of high-speed trains, Quarterly Report of RTRI, vol. 53, iss. 3, pp. 167–172, 2012. https://doi.org/10.2219/rtriqr.53.167

[3] C. J. Baker, The slipstream and wake of a high-speed train, Proceedings of the Institution of Mechanical Engineers, Part F: Journal of Rail and Rapid Transit, vol. 215, iss. 2, pp. 83–99, 2001. https://doi.org/10.1243/0954409011531422

[4] M. Yang, S. Zhong, L. Zhang, B. Quian, T. Wang, D. Zhiu, and F. Wu, 600 km/h moving model rig for high-speed train aerodynamics, Journal of Wind Engineering and Industrial Aerodynamics, vol. 227, Aug. 2022, Art. no. 105063. https://doi.org/10.1016/j.jweia.2022.105063

[5] H. Kwon, Y. Park, D. Lee, and M. Kim, Wind tunnel experiments on Korean high-speed trains using various ground simulation techniques, Journal of Wind Engineering and Industrial Aerodynamics, vol. 89, iss. 13, pp. 1179–1195, Oct. 2001. https://doi.org/10.1016/S0167-6105(01)00107-6

[6] J. Niu, Z. Dan, and L. Xi-feng, Experimental research on the aerodynamic characteristics of a high-speed train under different turbulence conditions, Experimental Thermal and Fluid Science, vol. 80, pp. 117–125, Jan. 2017. https://doi.org/10.1016/j.expthermflusci.2016.08.014

[7] F. Cheli, F. Ripamonti, D. Rocchi, and G. Tomasini, Aerodynamic behaviour investigation of the new EMUV250 train to cross wind, Journal of Wind Engineering Industrial Aerodynamics, vol. 98, iss. 4–5, pp. 189–201, Apr–May, 2010. https://doi.org/10.1016/j.jweia.2009.10.015

[8] G. Chen, X. Li, Z. Liu, D. Zhou, Z. Wang, X. Liang, and S. Krajnovic, Dynamic analysis of the effect of nose length on train aerodynamic performance, Journal of Wind Engineering and Industrial Aerodynamics, vol. 184, pp. 198–208, Aug. 2019. https://doi.org/10.1016/j.jweia.2018.11.021

[9] G. Gao, F. Li, K. He, J. Wang, J. Zhang, and X. Miao, Investigation of bogie positions on the aerodynamic drag and near wake structure of a high-speed train, Journal of Wind Engineering and Industrial Aerodynamics, vol. 185, pp. 41–53, Feb. 2019. https://doi.org/10.1016/j.jweia.2018.10.012

[10] C. Xia, H. Wang, X. Shan, Z. Yang, and Q. Li, Effects of ground configurations on the slipstream and near wake of a high-speed train, Journal of Wind Engineering and Industrial Aerodynamics, vol. 168, pp. 177–189, Sep. 2017. https://doi.org/10.1016/j.jweia.2017.06.005

[11] J. Zhang, K. Le, J. Wang, T. Liu, X. Liang, and G. Gao, Numerical simulation of flow around a high-speed train subjected to different windbreak walls and yaw angles, Journal of Applied Fluid Mechanics, vol. 12, iss. 4, pp. 1137–1149, Jul. 2019. https://doi.org/10.29252/jafm.12.04.29484